Enhancing Energy Product and Thermal Stability of $SmFe_{12}$ by Interstitial Doping

D. Odkhuu,[1,*] T. Ochirkhuyag,[1] and S. C. Hong[2,†]

[1] *Department of Physics, Incheon National University, Incheon 22012, South Korea*
[2] *Department of Physics, University of Ulsan, Ulsan 44610, South Korea*

(Received 26 September 2018; revised manuscript received 5 January 2019; accepted 17 April 2020; published 29 May 2020)

Enhancing energy product and thermal stability at the same time while retaining the concentration of rare-earth (RE) elements in RE-3*d* compounds is desirable for permanent magnetic applications. Herein, all-electron electronic structure calculations are used to reveal possibilities of enhancing saturation magnetization ($\mu_0 M_s$) and uniaxial magnetic anisotropy (K_u) in $ThMn_{12}$-type $SmFe_{12}$ by carefully exploring substitutional and interstitial impurities. More specifically, an addition of only one N atom, among 2*p*-electron elements, per formula unit cell of $SmFe_{12}$ not only improves its structural stability but also enhances K_u by more than 2 times and $\mu_0 M_s$ up to 5%, which are superior to those of the currently known permanent magnetic materials. Our calculations further demonstrate that these permanent magnetic properties of $SmFe_{12}$ can also be enhanced by replacing Fe with Co, in agreement with an experiment [Y. Hirayama *et al.*, Scr. Mater. 138, 62 (2017)].

DOI: 10.1103/PhysRevApplied.13.054076

I. INTRODUCTION

Inclusion of rare-earth (RE) elements in 3*d* transition metals (TMs) makes them desirable permanent magnetic materials because of their large uniaxial magnetic anisotropy (K_u) associated with the strong spin-orbit coupling (SOC) of 4*f* orbital shells [1,2]. However, RE elements, especially heavy RE elements, are very expensive and also detrimental to saturation magnetization (M_s) and Curie temperature (T_c) in 3*d* magnetic metals. Although there have been intensive research efforts to replace the 4*f* -3*d* compounds with RE-free magnets, no competitive magnetic materials have been identified thus far in terms of K_u. Instead, renewal of research targets seemingly resides in retaining or even enhancing M_s and K_u while reducing the atomic ratio of RE elements to 3*d* elements. In this context, $ThMn_{12}$-type $RETM_{12}$ compounds, where mainly RE = Sm or Nd and TM = Fe and/or Co, have been considered [3–13], owing to the reduced RE concentration with respect to the best permanent magnet $Nd_2Fe_{14}B$ [14–16]. In recent studies, for instance, simultaneous enhancements of K_u and $\mu_0 M_s$ (μ_0 is the vacuum permeability) as well as T_c have been reported in $ThMn_{12}$-type $SmFe_{12}$ by replacing up to 20% of Fe with Co [11], which are even superior to those of $Nd_2Fe_{14}B$ [14–16]. This is in sharp contrast to other TM substitutes, such as Ti, Mo, Cr, and V, where K_u and $\mu_0 M_s$ are greatly suppressed [4,5]. However, the thermal stability of $ThMn_{12}$-type phase, including $Sm(Fe_{1-x}Co_x)_{12}$, in bulk form is still insufficient for practical usage. In addition to the TM replacements, there have been several attempts to improve the stability of the $ThMn_{12}$ phase; for example, the presence of 2*p*-electron interstitial impurities stabilizes the $ThMn_{12}$ phase and also enhances $\mu_0 M_s$, where B, C, and N have been mainly utilized in most experiments undertaken thus far [17–21].

In this article, we report results of full-potential density-functional theory plus U (DFT+U) calculations and single-particle energy spectra analyses of simultaneous enhancements of K_u and $\mu_0 M_s$ in $ThMn_{12}$-type $SmFe_{12}$, which can be achieved by interstitial doping with N among 2*p*-electron elements (B, C, and N). It is further predicted that the presence of interstitial N dopant improves the structural stability in terms of the enthalpy of formation of the $ThMn_{12}$ phase. Moreover, in agreement with a recent experiment [11], the Co substitution for the Fe site in $SmFe_{12}$ can also enhance both K_u and $\mu_0 M_s$, which depends on a precise substitutional site of the Co element. The underlying mechanism is discussed in connection with the doping-induced modification in large spin-orbit-coupled 4*f* -orbital states, orbital magnetism, and 4*f* -2*p* and 4*f* -3*d* hybridizations.

II. COMPUTATIONAL METHODS

The density-functional Kohn-Sham equations are solved in a self-consistent manner using the full-potential

*odkhuu@inu.ac.kr
†schong@ulsan.ac.kr

WIEN2k method [22]. This method deals with both the core and valence electrons accurately and is suitable for magnetic systems. The exchange-correlation interactions are treated with the generalized gradient approximation (GGA) [23]. We use the muffin-tin radii of 1.02 Å for Fe and Co, 1.27 Å for Sm, and 0.90 Å for B, C, and N atoms, and $RK_{\max}$ value of 7. Herein, K_u is determined as $K_u = E_a - E_c$, where E_a and E_c are the total energies with magnetization along the a and c axes, respectively. For the k-point summation, 1271 k points (or $11 \times 11 \times 21$ k-point mesh) are used in the irreducible Brillouin zone (BZ). The convergence of K_u with respect to the number of k points is seriously checked. For the lattice and ionic coordinate relaxations, we employ the pseudopotential Vienna *ab initio* simulation package (VASP) [24] version 5.4.1. Energy cutoff of 600 eV, $7 \times 7 \times 13$ k-point mesh, and force criteria of 10^{-2} eV/Å are adopted. $4s^1 3d^7$, $4s^1 3d^8$, and $6s^2 5p^6 4f^6$ are treated as valence electrons for Fe, Co, and Sm, respectively. For both the VASP and WIEN2k methods, strongly correlated $4f$ electrons are treated with the Hubbard method, where the onsite Coulomb parameter U and Hund's exchange parameter J are chosen as 6 and 0 eV, respectively. The selection criterion of U_{eff} $(U - J)$ parameter is based on comparison of magnetic properties, especially K_u, with available experimental data, as addressed in the following section.

III. RESULTS AND DISCUSSION

The $ThMn_{12}$-type structure adopted for either $SmFe_{10}Co_2$ or $SmFe_{12}X$ (X = B, C, and N) is shown in Fig. 1. In this $ThMn_{12}$-type structure, two Sm atoms are located at the corner (denoted Sm_{a1}) and the center (denoted Sm_{a2}) in the Wyckoff position of $2a$, and 24 Fe atoms occupy three inequivalent sites, denoted Fe_f, Fe_i, and Fe_j, in the Wyckoff positions of $8f$, $8i$, and $8j$, respectively. In the optimized lattice, while the Fe_f site is equally separated by 3.22 Å from both Sm_{a1} and Sm_{a2}, the Sm_{a1}-Fe_i and Fe_i-Sm_{a2} (Sm_{a1}-Fe_j and Fe_j-Sm_{a2}) bond lengths are 3.06 and 4.98 Å (3.04 and 4.82 Å), respectively. Correspondingly, three distinctive substitutional configurations are considered, namely Co_f, Co_i, and Co_j. In each configuration, as one can build various distribution patterns of Co, we find that the Co substitutes prefer a uniform distribution, rather than that of one closer to another, from the total energy minimization (Fig. S1 in Supplemental Material [25]).

The standard DFT fails to accurately describe the strongly localized $4f$-orbital states due to the oversimplified treatment of electron correlations, where the $4f$-orbital states are pinned right at the Fermi level (E_F). This is also the case for the present system, as seen in the spin- and orbital-projected density of states (PDOS) of the Sm atom in $SmFe_{12}$ (topmost panel in Fig. 2). On the other hand, the DFT+U approach provides a more realistic treatment for the $4f$ states, as this splits the f-orbital bands into lower and upper Hubbard bands [26,27]. It is obvious from the Sm PDOS in Fig. 2 that the spin-down $4f$ bands at E_F are separated into occupied and unoccupied states by an amount U_{eff} in DFT+U.

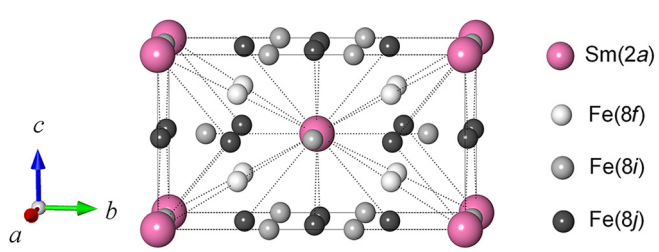

FIG. 1. Atomic structure of $ThMn_{12}$-type $SmFe_{12}$ adopted in the present calculations. The larger pink spheres denote the Sm atoms at the Wyckoff position $2a$, and the smaller white, gray, and black spheres are the Fe atoms at the Wyckoff positions $8f$, $8i$, and $8j$, respectively.

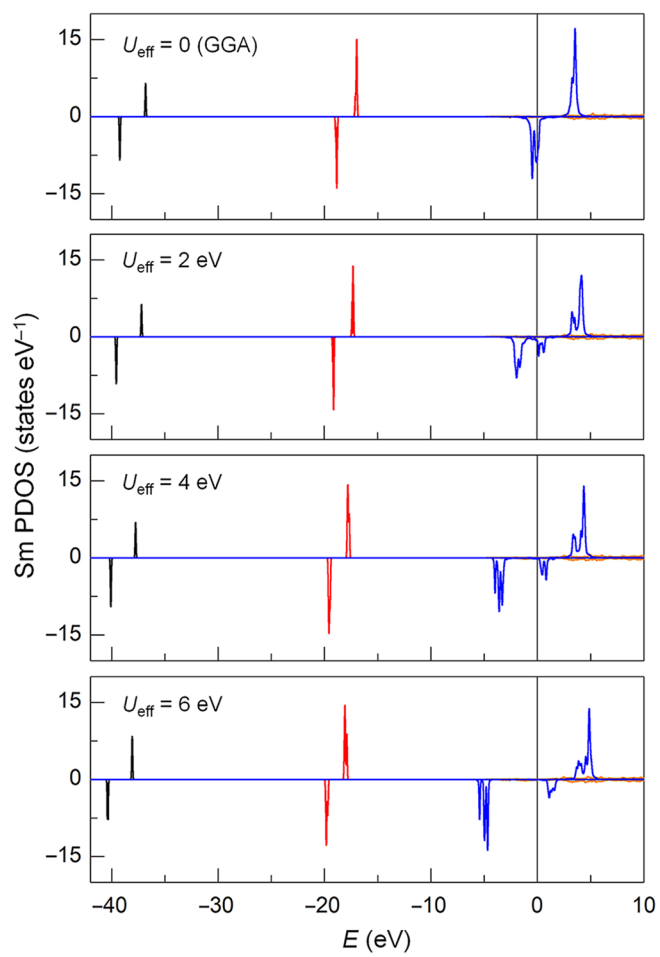

FIG. 2. PDOS of the s- (black), p- (red), d- (orange), and f-orbital (blue) states of the Sm atom in $SmFe_{12}$ from the standard DFT (topmost panel) and DFT+U method for different U_{eff} values. The Fermi level is set to zero in energy.

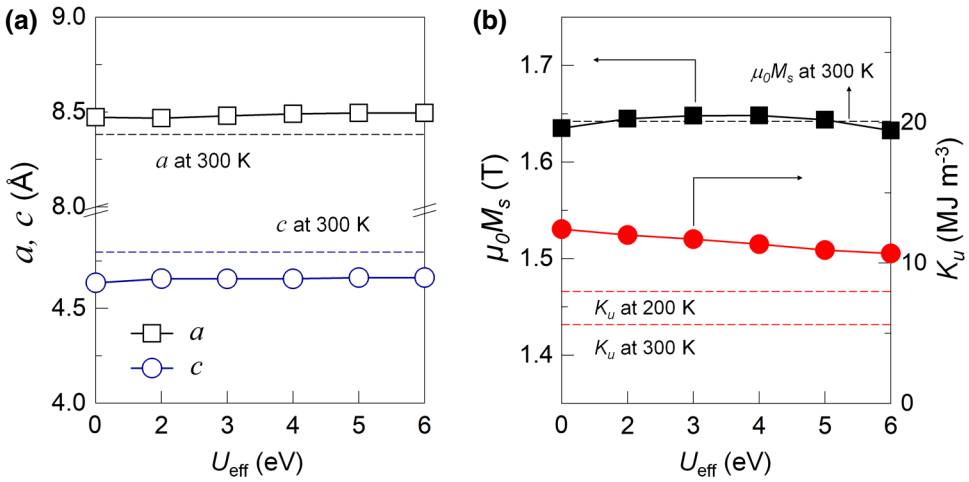

FIG. 3. (a) Optimized lattice parameters a and c and (b) saturation magnetization $\mu_0 M_s$ (left) and uniaxial magnetic anisotropy K_u (right) of $SmFe_{12}$ from the DFT+U method for different U_{eff} values. The corresponding experimental results measured at 200 and 300 K, taken from Ref. [11], are indicated by the horizontal dashed lines.

Nevertheless, in DFT+U it is ambiguous as to the proper choice of U_{eff} value. One practical way to determine U_{eff} is direct comparison with experimental data. With this in mind, we perform the DFT+U calculations of the structural and magnetic properties of $SmFe_{12}$ for different U_{eff} values. As shown in Fig. 3(a), the lattice parameters a and c, optimized using the VASP calculations, are almost independent of U_{eff} ranging from zero (DFT) to 6 eV. On the other hand, K_u ($\mu_0 M_s$) obtained from WIEN2k calculations decreases (slightly increases) as U_{eff} increases [Fig. 3(b)]. For the standard DFT, while $\mu_0 M_s$ (1.63 T) is comparable with a measured value of 1.64 T at room temperature [11], our computed K_u (12.4 MJ m^{-3}) is overestimated roughly 1.5–2 times compared with an experimental value of 5.4–8.0 MJ m^{-3} measured at 300–200 K. The inclusion of the U_{eff} parameter reduces such discrepancies and results in K_u of 10.6 MJ m^{-3} and $\mu_0 M_s$ of 1.63 T at $U_{\text{eff}} = 6$ eV, which we thus adapted for all calculations in the present study.

The optimized lattice parameters a and c, and volume V per formula unit (f.u.) cell of $SmFe_{12}$ and $SmFe_{10}Co_2$ compounds are listed in Table I for the Co_f, Co_i, and Co_j replacements. For $SmFe_{12}$, the calculated lattice constants a and c are 8.49 and 4.66 Å, respectively, in agreement with experimental results (8.44 and 4.81 Å) [4,11] and previous theoretical results (8.46–8.49 and 4.68–4.81 Å) [5,28]. These lattice parameters and volume do not change much (within 1%) upon Co insertion with similar atomic radii, as found in a recent experiment [11].

We next explore the structural stability of $ThMn_{12}$-phase $SmFe_{12}$ upon Co addition. The phase stability against phase decomposition into end-member compounds can be described thermodynamically by the change in the Gibbs free energy [29,30]: $\Delta G(T,P,N_i) = \Delta H(T,P,N_i) - T\Delta S(T,P,N_i) + P\Delta V(T,P,N_i)$, where H is the total energy of the system and T, S, P, and V are the temperature, entropy, pressure, and volume of the system, respectively. N_i is the number of atom species i in the system. In the present study, we follow the recipe proposed by Ong *et al.* [29,30], where the compositional phase diagram is constructed using the convex hull method. Since the $P\Delta V$ term is negligibly small and $\Delta G = \Delta H$ at $T = 0$ K, the phase stability can be formulated based on the enthalpy of formation:

$$H_f = \frac{H - \sum_k \mu_k N_k}{\sum_i N_i}, \tag{1}$$

where μ_k and N_k are the chemical potential and the number of decomposable compounds k, respectively. μ_k is estimated as the total energy of the ground-state structure.

In the Sm-Fe phase diagram, all Sm-Fe phases we studied, namely $SmFe_2$, $SmFe_5$, and $SmFe_{12}$, are not stable against α-Fe + bulk-Sm. Their enthalpies of formation are 5.78, 7.64, and 8.25 kJ mol^{-1}, respectively. This indicates that the $SmFe_{12}$ phase readily decomposes into intermetallic $SmFe_5$ phase and then $SmFe_2$ phase. A recent experiment reported the $SmFe_2$ phase as a competitive phase

TABLE I. Optimized lattice parameters a and c (Å) and volume V (Å ^{3}/f.u.) of $SmFe_{12}$ and $SmFe_{10}Co_2$ compounds for the Co_f, Co_i, and Co_j replacements.

	Co_f			Co_i			Co_j		
	a	c	V	a	c	V	a	c	V
$SmFe_{12}$	8.49	4.66	168.3	8.49	4.66	168.3	8.49	4.66	168.3
$SmFe_{10}Co_2$	8.51	4.67	169.2	8.49	4.65	167.6	8.48	4.67	167.7

to $SmFe_{12}$ [31]. Hence, for $SmFe_{12}$ and $SmFe_{10}Co_2$ compounds, we calculate the enthalpy of formation against α-Fe + $SmFe_2$ + *hcp*-Co decompositions, and results are presented in Fig. 4(a). In this convention, the obtained H_f of $SmFe_{12}$ is 3.84 kJ mol^{-1}, as its $ThMn_{12}$ phase is unstable in practice. On the other hand, the presence of the Co replacements improves the stability as H_f decreases in $SmFe_{10}Co_2$. In particular, the Co_f site, whose H_f is 0.44 kJ mol^{-1}, is more favored than the Co_i site by more than 2 kJ mol^{-1} and the Co_j site by more than 1 kJ mol^{-1}. Similar results are also predicted for $ThMn_{12}$-phase $NdFe_{11}Co$ [32].

Figure 4(b) shows the calculated $\mu_0 M_s$ of $SmFe_{12}$ and $SmFe_{10}Co_2$ for the Co_f, Co_i, and Co_j replacements. For $SmFe_{12}$, as mentioned above, the present computed result of $\mu_0 M_s$ (1.63 T) agrees fairly well with an experimental value of 1.64 T at room temperature [11]. With Co addition, $\mu_0 M_s$ is dependent on substitutional site: $\mu_0 M_s$ increases with Co_f and reaches 1.71 T for $SmFe_{10}Co_2$, while it tends to retain its value more or less for the Co_i and Co_j sites. In particular, our $\mu_0 M_s$ for the Co_f site, which is the most favorable substitutional site, exhibits a trend similar to that of experiments at room temperature, where $\mu_0 M_s$ increases from 1.64 T for $SmFe_{12}$ to 1.78 T for $Sm(Fe_{0.8}Co_{0.2})_{12}$ [11].

More remarkably, with this Co_f dopant site, in Fig. 4(c) we also find a similar trend for K_u enhancement as experiments at 200 (300) K from approximately 8 (5.4) MJ m^{-3} for $SmFe_{12}$ to approximately 8.2 (6.2) MJ m^{-3} for $Sm(Fe_{0.8}Co_{0.2})_{12}$ [11]. In our calculations, K_u increases from 10.6 MJ m^{-3} for $SmFe_{12}$ to 11.2 MJ m^{-3} for $SmFe_{10}Co_2$. Both the experimental magnetic anisotropy constants K_1 and K_2 increase as temperature decreases [cf. Fig. 3(c) in Ref. [11]]. In tetragonal symmetry, the uniaxial magnetic anisotropy can be expressed as $K_u = K_1 \sin^2\theta + K_2 \sin^4\theta + K_3 \sin^4\theta \cos 4\phi$, where K_1, K_2, and K_3 are the magnetic anisotropy constants, θ is the polar angle between the magnetization vector and the easy axis (c axis in the present system), and ϕ is the azimuthal angle between the magnetization component projected onto the ab plane and the a axis. In most cases, the higher term K_3 is relatively small compared with K_1 and K_2, and thus not often considered. For $\theta = \pi/2$, $K_u \approx K_1 + K_2$.

In Fig. 4(d), we show the calculated orbital magnetic anisotropy (ΔM_L) of $SmFe_{12}$ and $SmFe_{10}Co_2$ for the Co_f, Co_i, and Co_j replacements. Here, ΔM_L is defined as

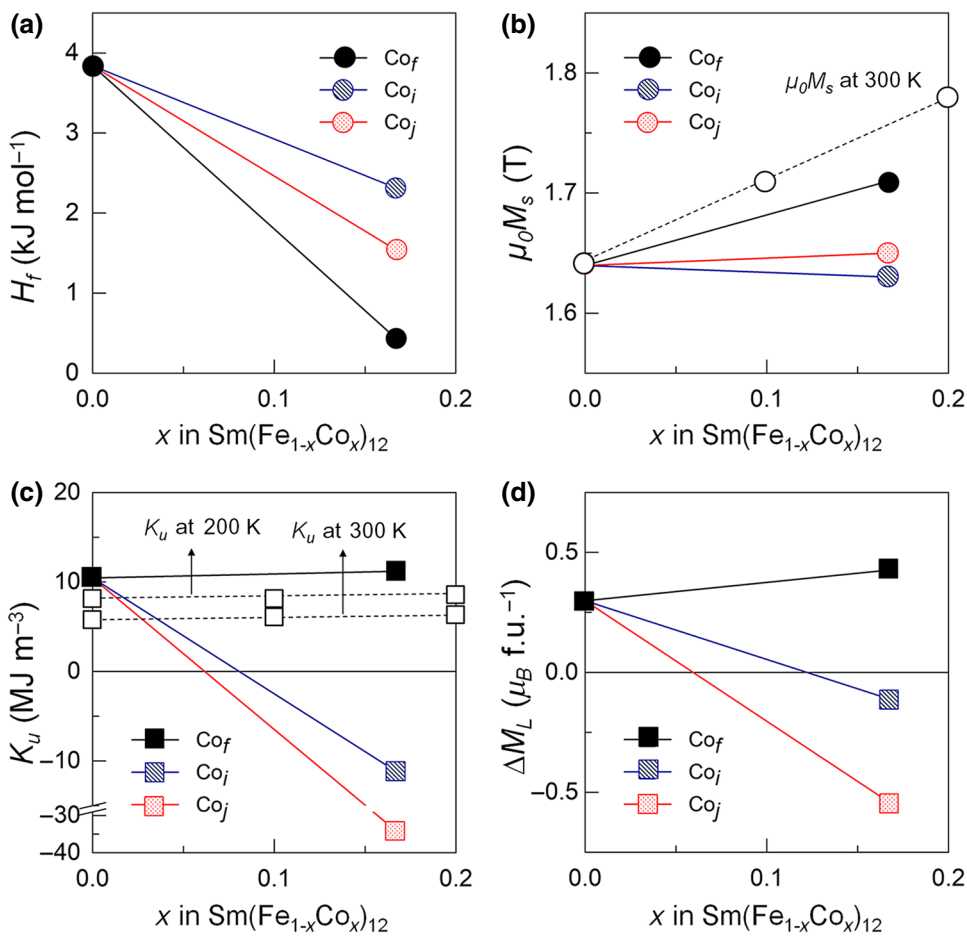

FIG. 4. (a) Enthalpy of formation H_f, (b) saturation magnetization $\mu_0 M_s$, (c) uniaxial magnetic anisotropy K_u, and (d) orbital moment anisotropy ΔM_L of $SmFe_{12}$ and $SmFe_{10}Co_2$ compounds for the Co_f, Co_i, and Co_j replacements. Open symbols in (b) and (c) represent the corresponding experimental values at 200 and 300 K, taken from Ref. [11].

$\Delta M_L = (M_L)_c - (M_L)_a$, where $(M_L)_c$ and $(M_L)_a$ are the total orbital magnetic moments along the c and a axes, respectively, Overall, K_u and ΔM_L correlate well through the Bruno expression $K_u = (\xi/4\mu_B)\Delta M_L$ [33], where ξ is the strength of SOC.

To understand the enhanced $\mu_0 M_s$ on Co addition, we show the local spin magnetic moment (m_s) and charge difference ($\Delta\Omega$) with respect to the nominal charge of $SmFe_{12}$ and $SmFe_{10}Co_2$ with the Co_f replacement in Figs. 5(a) and 5(b), respectively. The nominal charges of the Fe, Co, and Sm atoms are 8, 9, and 16 e, respectively. In an ideal case, the spin moment of the individual Sm is 6 μ_B for the $4f^6$ orbitals in the high-spin state according to Hund's first rule. The present Sm moment (-5.23 μ_B) of $SmFe_{12}$ is found to be somehow smaller in magnitude because of its charge depletion to the Fe sites. Furthermore, the magnetic moments of the Fe_f, Fe_i, and Fe_j sites are 1.76, 2.50, and 2.28 μ_B, respectively. The Fe_f and Fe_j atoms gain 0.26 and 0.13 e, respectively, while the Fe_i site loses -0.10 e. This charge redistribution results in the reduced moment of the Fe_f site and the enhanced moment of the Fe_i site with respect to the bulk Fe moment (2.2 μ_B). The antiparallel coupling of the Sm $4f$ to the Fe $3d$ moments is mediated by the Sm $5d$ orbitals, whose spin is parallel to the $4f$ but antiparallel to the $3d$ through their orbital hybridizations [34].

The presence of the Co_f replacement, whose spin magnetic moment is 1.38 μ_B, reduces the Sm moment (-5.13 μ_B) in magnitude [Fig. 5(a)]. On the other hand, the Co_f atom accumulates a charge of 0.50 e mainly from its neighboring Fe_f (0.10 e/atom) and 4 Fe_j (0.03 e/atom) atoms. This in turn enhances the Fe_f (2.1 μ_B) and Fe_j (2.4 μ_B) moments, and thus $\mu_0 M_s$ increases. Moreover, the orbital moment contribution of the Sm to $\mu_0 M_s$ is substantial. We find notable m_L values of 2.18 and 2.25 μ_B for the Sm $4f$ orbitals of $SmFe_{12}$ and $SmFe_{10}Co_2$, respectively, antiparallel to the spin moment. The antiparallel orientation of the orbital angular momentum (L) to the spin angular momentum (S) is according to Hund's third rule for the less-than-half-filled Sm $4f$ shell. In contrast, those of the Fe sites are rather small, less than 0.05 μ_B.

To elucidate the origin of large K_u and its further enhancement by the Co replacement, we analyze the atom-resolved K_u and ΔM_L in Figs. 5(c) and 5(d), respectively. For $SmFe_{12}$, the Sm, Fe_f, Fe_i, and Fe_j atoms have K_u contributions of $+9.80$, -0.21, -0.03, and $+0.12$ meV to the total K_u of $+9.32$ meV/f.u. Those of $SmFe_{10}Co_2$ ($+11.82$ meV/f.u.) are $+11.12$, -0.09, $+0.04$, $+0.10$ meV, respectively, while the Co_f has K_u of -0.16 meV. The obtained ΔM_L values of the Sm atom are 0.22 and 0.35 μ_B for $SmFe_{12}$ and $SmFe_{10}Co_2$, respectively. On the other hand, the contributions from the Fe and Co sites to ΔM_L

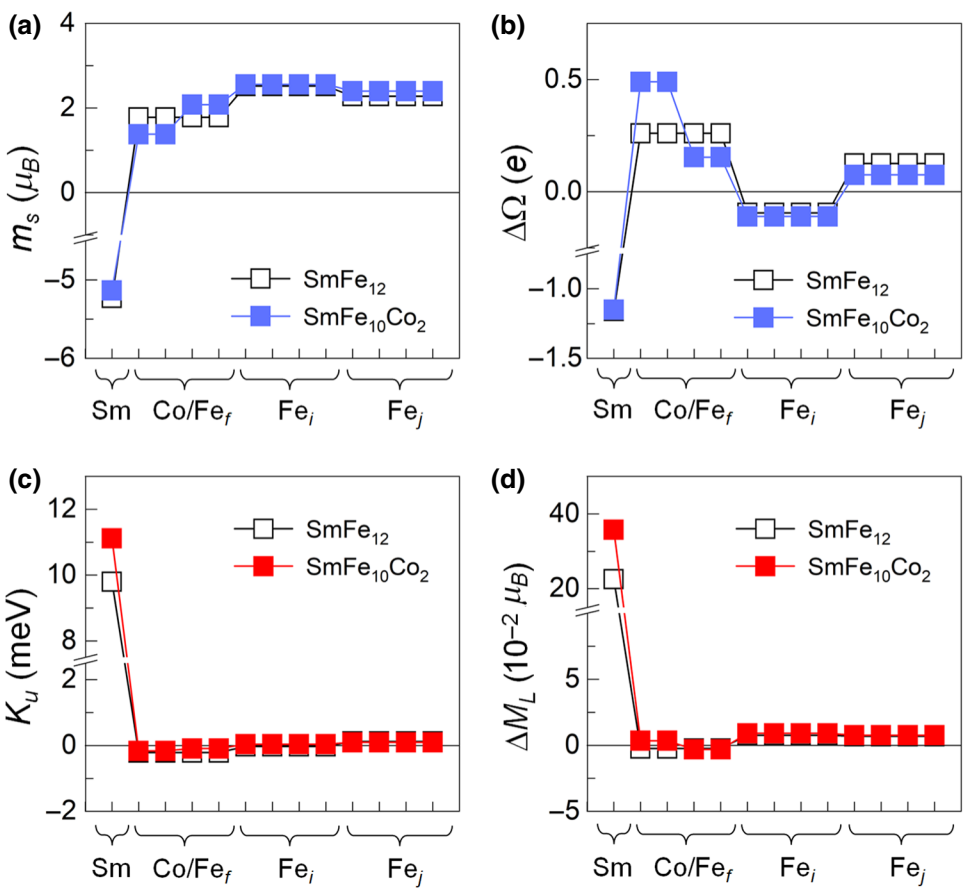

FIG. 5. Atom-resolved (a) spin magnetic moment m_s, (b) charge difference $\Delta\Omega$, (c) magnetic anisotropy K_u, and (d) orbital moment anisotropy ΔM_L of $SmFe_{12}$ and $SmFe_{10}Co_2$ compounds.

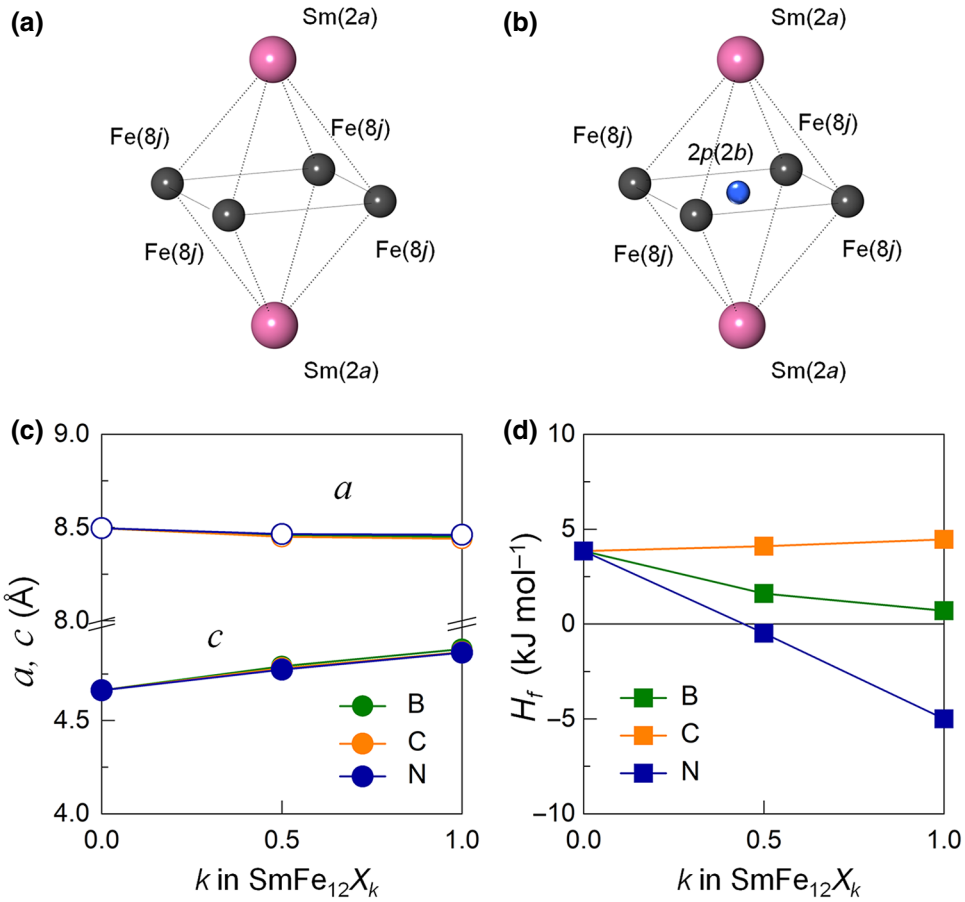

FIG. 6. Schematic diagrams representing (a) octahedron surrounded by the Sm(2a) and Fe(8j) atoms and (b) 2b site of 2p-dopant atom (X) at the center of octahedron in $ThMn_{12}$-type $SmFe_{12}$. The larger pink and black spheres denote the Sm and Fe atoms, respectively. The smaller blue sphere denotes the 2p-dopant atom. (c) Optimized lattice parameters a (open circles) and c (filled circles) and (d) the enthalpy of formation H_f of $SmFe_{12}X_k$ as function of k concentration for X = B (green), C (orange), and N (blue).

are insignificant, of the order of 10^{-3} μ_B. The spin-orbit effect as a physical origin of anisotropic phenomena is thus simply justified with the inherently large SOC of the Sm 4f orbitals.

As the relative energy levels of the Sm 4f orbitals are determinant for K_u, one might speculate to explore the possible engineering of K_u through 4f-2p hybridization. We here consider B, C, and N elements as interstitial impurities in $SmFe_{12}$, as they have been utilized in most experiments undertaken thus far [17–21]. For each dopant, the most favorable interstitial site is determined as the 2b site in our total energy calculations, as illustrated in Figs. 6(a) and 6(b). Experiments also reported that 2p dopants occupy the interstitial 2b site [17–21]. Furthermore, it has been experimentally shown that $SmFe_{12}$ can accommodate 2p dopants, for the case of N, up to 1 atom/f.u. and still retain the $ThMn_{12}$ structure [35,36]. The optimized lattice parameters a and c and volume V of $SmFe_{12}X_k$ as function of k are shown in Fig. 6(c) for X = B, C, and N. The presence of X dopants does not change much the lattice constant a (reduced less than 1%), but enhances the lattice constant c by approximately 4%–5% at $k = 1$ (and hence the volume by approximately 2.5%–4%).

Figure 6(d) displays the enthalpy of formation of $SmFe_{12}X_k$ as function of k for X = B, C, and N. Here, the enthalpy of formation H_f is calculated against α-Fe+$SmFe_2$ + N_2 decompositions through $H_f = H(SmFe_{12}X_k) - H(SmFe_2) - 10 \times H(Fe) - k \times H(X)$, where $H(SmFe_{12}X_k)$, $H(SmFe_2)$, $H(Fe)$, and $H(X)$ are the total energies of $SmFe_{12}X_k$, $SmFe_2$, Fe, and X atoms in their ground-state phases (i.e., α-Fe, α-rhombohedral boron, graphitic carbon, and N_2 molecule), respectively. Our calculations show that, in contrast to C, B and N improve stability of the $ThMn_{12}$ phase. In particular, H_f of $SmFe_{12}N_k$ decreases with k and changes its sign from positive to negative, reaching -4.9 kJ mol^{-1} at $k = 1$. The negative H_f means the favorable formation of the single-crystalline $ThMn_{12}$ structure against the phase separation into the intermetallic $SmFe_2$ and α-Fe decompositions. Note that $SmFe_{12}N$ might decompose into the SmN and FeN phases at an elevated temperature, according to the ternary phase diagram of Sm-Fe-N compounds provided in the Materials Project Database [37,38]. Nevertheless, it should be emphasized that the Sm_2Fe_{17} phase, which is unstable under ambient conditions, has been achieved in the $Sm_2Fe_{17}N_3$ form [39–42]. One can thus expect the same situation for the present system.

In Table II, we present the calculated $\mu_0 M_s$ and K_u of $SmFe_{12}X$ for X = B, C, and N. Most remarkably, among the X dopants, only N enhances both $\mu_0 M_s$ and

TABLE II. Saturation magnetization $\mu_0 M_s$ (T), uniaxial magnetic anisotropy K_u (MJ m^{-3}), theoretical energy product $(BH)_{\max}$ (MGOe), and hardness parameter κ of $SmFe_{12}X$ compounds for X = B, C, and N. The corresponding results for $SmFe_{12}$ are also shown for comparison.

	$\mu_0 M_s$	K_u	$(BH)_{\max}$	κ
$SmFe_{12}$	1.63	10.6	67.1	2.24
$SmFe_{12}B$	1.63	−31.6	66.5	...
$SmFe_{12}C$	1.60	−33.5	63.4	...
$SmFe_{12}N$	1.72	28.1	74.2	3.46

K_u simultaneously. More specifically, $SmFe_{12}N$ exhibits $\mu_0 M_s$ as high as 1.72 T, which is an approximately 5% enhancement compared with that (1.63 T) of $SmFe_{12}$. Indeed, the enhancement of $\mu_0 M_s$ by an interstitial N is quite typical in other RE-included magnets; for example, $NdFe_{12}N$ [6,17,18] and $Sm_2Fe_{17}N_3$ [39,40], where the quantitative increments are 5% and 12%, respectively. Furthermore, in recent studies of $ThMn_{12}$-type $NdFe_{12}$, the presence of N is shown to enhance $\mu_0 M_s$ most among the other $2p$ dopants including B and C [7,8].

Figures 7(a) and 7(b) show the atom-resolved m_s and $\Delta\Omega$ of $SmFe_{12}X$ for X = B, C, and N. The N dopant enhances the Fe_f (2.08 μ_B) and Sm (−5.11 μ_B) moments, which in $SmFe_{12}$ are 1.78 and −5.23 μ_B, more than the B dopant (1.91 and −5.19 μ_B) and the C dopant (1.83 and −5.61 μ_B). This in turn yields the largest $\mu_0 M_s$ of $SmFe_{12}N$ among the $SmFe_{12}X$ compounds. From the charge analyses in Fig. 7(b), while the charge of the Fe_i site remains almost unchanged, significant charge transfer occurs from the Sm, Fe_f, and Fe_j sites to the X dopants. This is because of the larger electronegativities of $2p$ elements (2.04–3.44) than Sm (1.17) and Fe (1.83). Moreover, the induced moment (0.12 μ_B) of the N dopant is parallel to the Fe moments, in contrast to the negative spin moments of the B (−0.14 μ_B) and C (−0.18 μ_B) dopants.

To a certain extent, the enhancement in $\mu_0 M_s$ of $SmFe_{12}N$ could also be partly correlated to a volume expansion upon N insertion [41]. Our fixed volume calculations show that $\mu_0 M_s$ of $SmFe_{12}$ with an enhanced volume of 2.5%, which corresponds to the optimized volume (172.34 Å^3/f.u.) of $SmFe_{12}N$, is 1.68 T [Fig. S2(a) [25]]. This volume-only induced enhancement (0.04 T) is essentially a half of the total enhancement of 0.08 T on N insertion. On the other hand, as shown in Fig. S2(b) [25], K_u dependence on volume exhibits a trend opposite to that of $\mu_0 M_s$, where K_u decreases from 10.6 to 9.5 MJ m^{-3} with a 2.5% enhancement in volume. This reduced K_u can be presumably associated with the lowered tetragonal distortion c/a, from 0.55 for $SmFe_{12}$ to 0.57 for $SmFe_{12}N$.

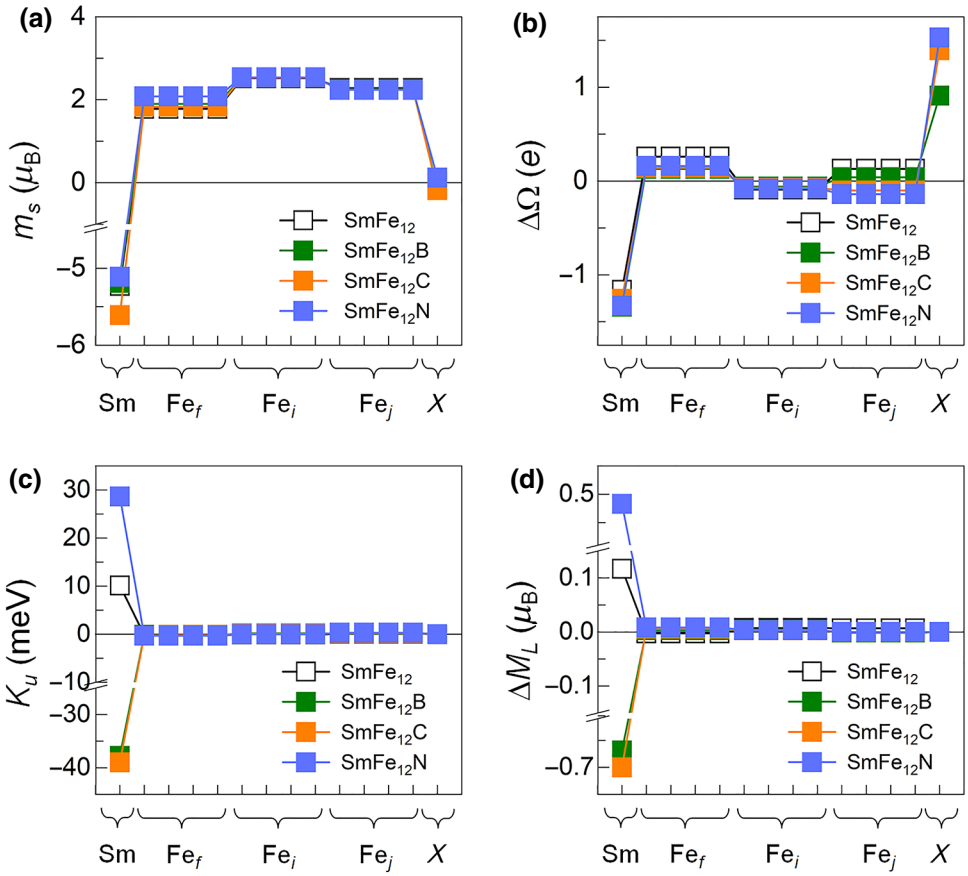

FIG. 7. Atom-resolved (a) spin magnetic moment m_s, (b) charge difference $\Delta\Omega$, (c) magnetic anisotropy K_u and (d) orbital moment anisotropy ΔM_L of $SmFe_{12}X$ compounds for X = B, C, and N.

In our prediction, $ThMn_{12}$-phase $SmFe_{12}N$ exhibits an extremely large K_u of 28.1 $MJ\,m^{-3}$ (Table II), which is more than 2 times larger than that (10.6 $MJ\,m^{-3}$) of $SmFe_{12}$. In low-temperature experiments of $NdFe_{12}$, an addition of 1 N atom/f.u. was reported to enhance K_u by more than 2 times, from 6.75 $MJ\,m^{-3}$ for $NdFe_{12}N_{0.5}$ [17] to 18 $MJ\,m^{-3}$ for $NdFe_{12}N_{1.5}$ [18]. It should also be noted that an order-of-magnitude enhancement in K_u was reported for Sm_2Fe_{17} when doped with N in both experiment [39] and previous theory [42]. Our prediction for $SmFe_{12}N$ would thus agree at least qualitatively with the results of low-temperature experiments. However, practical K_u (or enhancement) at an elevated temperature would possibly be smaller than prediction, as both K_1 and K_2 dramatically decrease with temperature [11]. In addition, the theoretical energy product $(BH)_{\max}$, defined as $(BH)_{\max} = (1/4)\mu_0 M_s^2$, and hardness parameter κ, $\kappa = (K_u/\mu_0 M_s^2)^{1/2}$, of $SmFe_{12}$ and $SmFe_{12}X$ compounds are also presented in Table II.

From atom-decomposed K_u and ΔM_L in Figs. 7(c) and 7(d), the Bruno model is approximately satisfied. The calculated values of K_u (ΔM_L) of the Sm atom are −37.8 (−0.67), −39.4 (−0.70), and 28.7 meV (0.48 μ_B) for $SmFe_{12}B$, $SmFe_{12}C$, and $SmFe_{12}N$, respectively. Even though the contribution of the Sm atom to K_u is dominant, the contribution of the Fe_j site, which is first nearest neighbor to the X dopant with a separation of 1.90–1.92 Å, to the X-induced changes in K_u cannot be ignored. For example, for $SmFe_{12}N$, the Fe_j site has K_u of 0.34 meV, which is almost 4 times larger than that (0.09 meV) for $SmFe_{12}$. The other two Fe_f and Fe_i sites, which are separated from N by 3.22 and 3.88 Å, retain K_u almost as those in $SmFe_{12}$.

Figure 8 provides PDOS of the Sm $4f$ and X $2p$ orbital states for $SmFe_{12}$, $SmFe_{12}B$, and $SmFe_{12}N$ compounds. Only the X p_z orbital state is emphasized as the changes of the other orbital states upon $4f$-$2p$ hybridization are insignificant (Fig. S3 in the Supplemental Material [25]). Apparently, for $SmFe_{12}$, the six $4f$ orbitals are filled only by the minority-spin electrons (↓) in the high-spin state, while the majority-spin states (↑) are completely empty (hence, the Sm site spin moment of −5.23 μ_B). Obviously, as produced by the $4f$-$2p$ hybridization in $SmFe_{12}N$, the PDOS peak states of the Sm f_0 and N p_z states around E_F are most prominent, as indicated in the inset in Fig. 8. Thereby, these newly developed ↑ f_0 bands below E_F and ↓ f_0 bands above E_F should be involved for SOC pairs that provide an additional positive contribution to K_u. This applies oppositely for $SmFe_{12}B$, as the empty ↓ f_0 band disappears. Instead, the occurrence of the ↓ $f_{\pm1}$ peak states around 1 eV, as a result of the Sm $4f$-B $2p$ hybridization, enhances negative contribution by $\langle\downarrow f_0|\downarrow f_{\pm1}\rangle$ and/or $\langle\downarrow f_{\pm2}|\downarrow f_{\pm1}\rangle$. Moreover, the ↑ Fe_j $d_{xz,yz}$ and ↑ Fe_j $d_{x^2-y^2}$ peak states of $SmFe_{12}N$ across E_F, which are not present for $SmFe_{12}$ and $SmFe_{12}B$, are also responsible for enhanced K_u at the Fe_j site [43]. This argument is more clearly supported by PDOS analyses of the Fe_f, Fe_i, and Fe_j sites in the Supplemental Material (Figs. S4–S6 [25]).

Finally, *ab initio* molecular dynamics (AIMD) simulation is used to investigate the structural stability and magnetization of $SmFe_{12}N$ at an elevated temperature. Figures 9(a) and 9(b) show the AIMD fluctuations of the total energy (ΔE) and spin magnetization (Δm_s), with respect to those of the first time step at 0 K, of $SmFe_{12}$ and $SmFe_{12}N$ during the AIMD simulation time of 5000 fs with 10 000

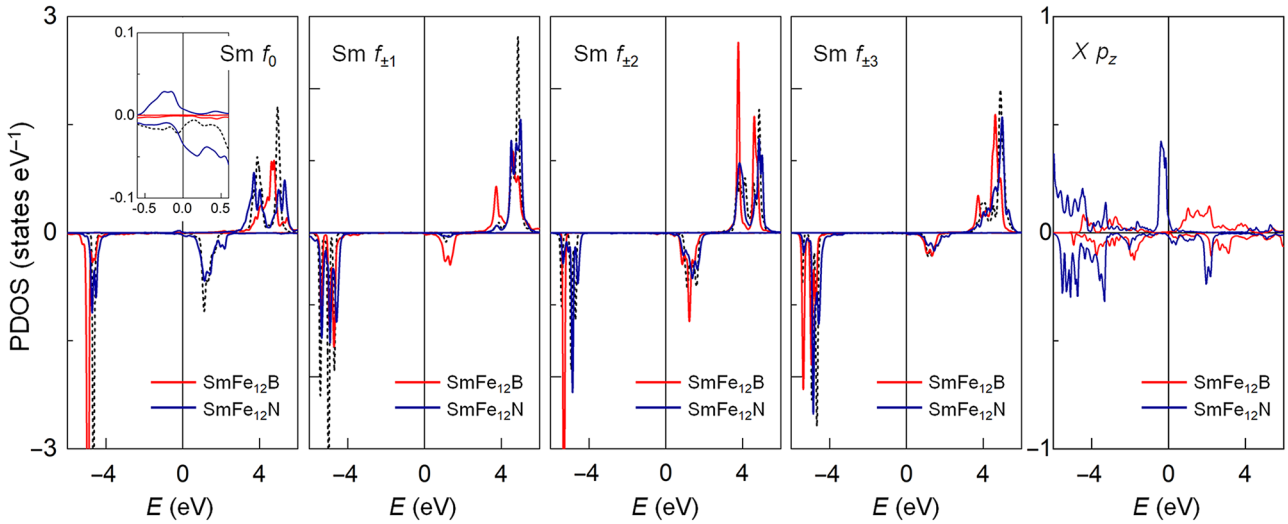

FIG. 8. Orbital-resolved PDOS of the Sm $4f$ and X $2p$ (X = B and N) states of $SmFe_{12}B$ (solid red line) and $SmFe_{12}N$ (solid blue line). The same for $SmFe_{12}$ are also shown in the dashed black line. The inset in the leftmost panel shows the same PDOS of Sm f_0 orbital states in the reduced energy and state scale ranges around the Fermi level for better readability. The Fermi level is set to zero in energy.

ionic steps for given temperatures 0, 300, and 500 K. All the AIMD calculations are performed with the Γ-point BZ integration at constant volume. For $SmFe_{12}$, while the total energy is enhanced with temperature, Δm_s decreases and reaches approximately $-2\ \mu_B$/f.u., which corresponds to roughly -0.28 T if the contribution of the orbital magnetic moments is fixed, at 500 K. Experiment reported that $\mu_0 M_s$ decreases from 1.63 T at 300 K to about 1 T at 500 K [11]. On the other hand, when temperature increases from 0 to 500 K, the total energy of $SmFe_{12}N$ is lowered by 0.07 eV/f.u. and the total magnetization is reduced by up to 2 μ_B/f.u. [Fig. 9(b)]. Such an energy gain is mainly associated with the relocation of the N dopant atoms at elevated temperatures. As indicated in Fig. 9(c), the N atom relocates from its original 2*b* position by 0.5–0.8 Å after the AIMD simulation period of 5 ps at 300–500 K, while the other atoms displace within 0.4 Å. The $ThMn_{12}$ phase is still maintained even at 500 K, although there is a tenuous phonon vibration during the AIMD steps.

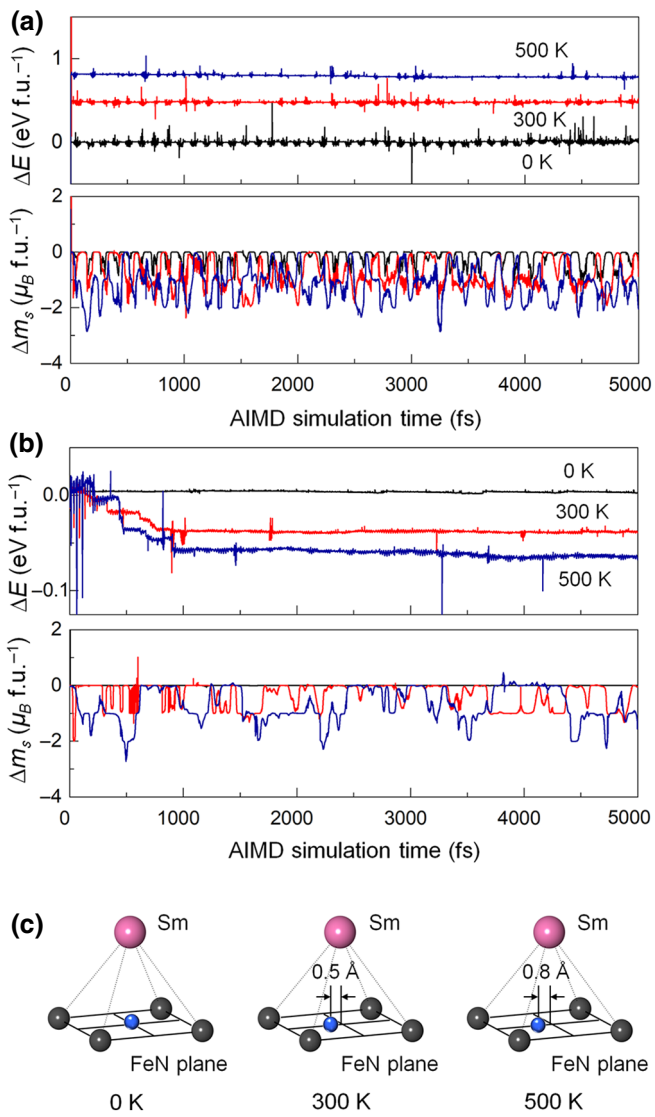

FIG. 9. AIMD fluctuations of the total energy ΔE and spin magnetization Δm_s of (a) $SmFe_{12}$ and (b) $SmFe_{12}N$ for given temperatures 0, 300, and 500 K. (c) Schematic diagram representing the relative displacement of the N dopant (blue sphere) on the FeN plane to the Sm atom (pink sphere) after the AIMD simulation period of 5 ps for 0, 300, and 500 K.

IV. CONCLUSION

In summary, using first-principles calculations and single-particle energy spectral analyses, we have predicted enhancements of $\mu_0 M_s$ and K_u in $ThMn_{12}$-type $SmFe_{12}$ by an interstitial doping with 2*p*-electron elements. In terms of the structural stability and energy product, the presence of an interstitial N dopant is most desirable. Furthermore, our calculations provide insights into the recent experiments concerning the enhanced $\mu_0 M_s$ and K_u of $SmFe_{12}$ by replacing the Fe site with Co. These results would thus suggest a viable route for enhancing simultaneously structural phase stability and intrinsic hard magnetic properties by carefully replacing Fe with 3*d* elements and interstitial dopants in $ThMn_{12}$-type compounds. We hope that our prediction inspires subsequent experimental and theoretical investigations of high-efficiency permanent magnetic materials with the $ThMn_{12}$ structure.

ACKNOWLEDGMENTS

This work is supported by Future Materials Discovery Program through the National Research Foundation of Korea (NRF) funded by the Ministry of Science and ICT (2016M3D1A1027835) and by the Korea Institute of Energy Technology Evaluation and Planning (KETEP) grant funded by the Korean government (MOTIE) (20192010106850, development of magnetic materials for IE4 class motor).

[1] K. H. J. Buschow in *Handbook on the Physics and Chemistry of Rare Earths*, edited by K. A. Gschneidner, Jr. and L. Eyring (North-Holland, Amsterdam, 1984).

[2] J. M. D. Coey, J. M. Cadogan, and D. H. Ryan, in Nd-Fe *Permanent Magnets: Their Present and Future Applications*, edited by I. V. Mitchell (Elsevier Applied Science, London/New York, 1985).

[3] S. F. Cheng, V. K. Sinha, Y. Xu, J. M. Elbicki, E. B. Boltich, W. E. Wallace, S. G. Sankar, and D. E. Laughlin, Magnetic and structural properties of $SmTiFe_{11-x}Co_x$ alloys, J. Magn. Magn. Mater. **75**, 330 (1988).

[4] F. J. Cadieu, H. Hegde, A. Navarathna, R. Rani, and K. Chen, High-energy product $ThMn_{12}$ Sm-Fe-T and Sm-Fe permanent magnets synthesized as oriented sputtered films, Appl. Phys. Lett. **59**, 875 (1991).

[5] C. N. Xian, H. S. Qiang, W. Yu, and S. Jiang, Phase stability and site preference of $Sm(Fe, T)_{12}$, J. Magn. Magn. Mater. **233**, 169 (2001).

[6] T. Miyake, K. Terakura, Y. Harashima, H. Kino, and S. Ishibashi, First-principles study of magnetocrystalline anisotropy and magnetization in $NdFe_{12}$, $NdFe_{11}Ti$, and $NdFe_{11}TiN$, J. Phys. Soc. Jpn. **83**, 043702 (2014).

[7] Y. Harashima, K. Terakura, H. Kino, S. Ishibashi, and T. Miyake, Nitrogen as the best interstitial dopant among X = B, C, N, O, and F for strong permanent magnet $NdFe_{11}TiX$: First-principles study, Phys. Rev. B **92**, 184426 (2015).

[8] T. Fukazawa, H. Akai, Y. Harashima, and T. Miyake, First-principles study of intersite magnetic couplings in $NdFe_{12}$ and $NdFe_{12}X$ (X = B, C, N, O, F), J. Appl. Phys. **122**, 053901 (2017).

[9] Y. Hirayama, Y. Takahashi, S. Hirosawa, and K. Hono, $NdFe_{12}N_x$ hard-magnetic compound with high magnetization and anisotropy field, Scr. Mater. **95**, 70 (2015).

[10] W. Korner, G. Krugel, and C. Elsasser, Theoretical screening of intermetallic $ThMn_{12}$-type phases for new hard-magnetic compounds with low rare earth content, Sci. Rep. **6**, 24686 (2016).

[11] Y. Hirayama, Y. K. Takahashi, S. Hirosawa, and K. Hono, Intrinsic hard magnetic properties of $Sm(Fe_{1-x}Co_x)_{12}$ compound with the $ThMn_{12}$ structure, Scr. Mater. **138**, 62 (2017).

[12] C. Skelland, T. Ostler, S. C. Westmoreland, R. F. L. Evans, R. W. Chantrell, M. Yano, T. Shoji, A. Manabe, A. Kato, M. Ito, M. Winklhofer, G. Zimanyi, J. Fischbacher, T. Schrefl, and G. Hrkac, Probability distribution of substituted titanium in RT_{12} (R = Nd and Sm; T = Fe and Co) structures, IEEE Trans. Magn. **54**, 2103405 (2018).

[13] T. Fukazawa, H. Akai, Y. Harashima, and T. Miyake, First-principles study of spin-wave dispersion in $Sm(Fe_{1-x}Co_x)_{12}$, J. Magn. Magn. Mater. **469**, 296 (2019).

[14] S. Hirosawa, Y. Matsuura, H. Yamamoto, S. Fujimura, M. Sagawa, and H. Yamauchi, Single crystal measurements of anisotropy constants of $R_2Fe_{14}B$ (R = Y, Ce, Pr, Nd, Gd, Tb, Dy and Ho), Jpn. J. Appl. Phys. **24**, L972 (1985).

[15] M. Sagawa, S. Fujimura, H. Yamamoto, Y. Matsuura, and S. Hirosawa, Magnetic properties of rare-earth-iron-boron permanent magnet materials, J. Appl. Phys. **57**, 4094 (1985).

[16] J. F. Herbst, $R_2Fe_{14}B$ materials: Intrinsic properties and technological aspects, Rev. Mod. Phys. **63**, 819 (1991).

[17] Y. C. Yang, X. D. Zhang, L. S. Kong, Q. Pan, and S. L. Ge, New potential hard magnetic material - $NdTiFe_{11}N_x$, Solid State Commun. **78**, 317 (1991).

[18] M. Akayama, H. Fujii, K. Yamamoto, and K. Tatami, Physical properties of nitrogenated $RFe_{11}Ti$ intermetallic compounds (R = Ce, Pr and Nd) with $ThMn_{12}$-type structure, J. Magn. Magn. Mater. **130**, 99 (1994).

[19] D. P. F. Hurley and J. M. D. Coey, Gas-phase interstitially modified intermetallics $R(Fe_{11}Ti)Z_{1-\delta}$. I. Magnetic properties of the series $R(Fe_{11}Ti)C_{1-\delta}$: R = Y, Nd, Sm, Gd, Tb, Dy, Ho, Er, Tm, Lu, J. Phys.: Condens. Matter **4**, 5573 (1992).

[20] J. Yang, P. Oleinek, D. Eckert, M. Wolf, and K.-H. Muller, Effect of interstitial carbon on the structural and magnetic properties of $Nd(Fe, M)_{12}C_y$ (M = Ti, V, Mo), J. Magn. Magn. Mater. **214**, 44 (2000).

[21] S. A. Nikitin, I. S. Tereshina, V. N. Verbetsky, and A. A. Salamova, Transformation of magnetic phase diagram as a result of insertion of hydrogen and nitrogen atoms in crystalline lattice of $RFe_{11}Ti$ compounds, J. Alloy. Comp. **316**, 46 (2001).

[22] P. Blaha, K. Schwarz, G. K. H. Madsen, D. Kvasnicka, and J. Luitz, *WIEN2k, An Augmented Plane Wave + Local Orbitals Program for Calculating Crystal Properties* (Techn. Universitat Wien, Vienna, 2001).

[23] J. P. Perdew, J. A. Chevary, S. H. Vosko, K. A. Jackson, M. R. Pederson, D. J. Singh, and C. Fiolhais, Atoms, molecules, solids, and surfaces: Applications of the generalized gradient approximation for exchange and correlation, Phys. Rev. B **46**, 6671 (1992).

[24] G. Kresse and J. Hafner, Ab initio molecular dynamics for liquid metals, Phys. Rev. B **47**, 558(R) (1993).

[25] See supplemental material at http://link.aps.org/supplemental/10.1103/PhysRevApplied.13.054076 for the detailed energetics, magnetic properties, and electronic structure analyses.

[26] P. Larson, I. I. Mazin, and D. A. Papaconstantopoulos, Calculation of magnetic anisotropy energy in $SmCo_5$, Phys. Rev. B **67**, 214405 (2003).

[27] T. Pandey, M.-H. Du, and D. S. Parker, Tuning the Magnetic Properties and Structural Stabilities of the 2-17-3 Magnets $Sm_2Fe_{17}X_3$ (X = C, N) by Substituting La or Ce for Sm, Phys. Rev. Appl. **9**, 034002 (2018).

[28] P. Delange, S. Biermann, T. Miyake, and L. Pourovskii, Crystal-field splittings in rare-earth-based hard magnets: An ab initio approach, Phys. Rev. B **96**, 155132 (2017).

[29] S. P. Ong, L. Wang, B. Kang, and G. Ceder, Li-Fe-P-O_2 phase diagram from first principles calculations, Chem. Mater. **20**, 1798 (2008).

[30] S. P. Ong, A. Jain, G. Hautier, B. Kang, and G. Ceder, Thermal stabilities of delithiated olivine MPO_4 (M = Fe, Mn) cathodes investigated using first principles calculations, Electrochem. Commun. **12**, 427 (2010).

[31] I. Dirba, Y. Harashima, H. Sepehri-Amin, T. Ohkubo, T. Miyake, S. Hirosawa, and K. Hono, Thermal decomposition of $ThMn_{12}$-type phase and its optimum stabilizing elements in $SmFe_{12}$-based alloys, J. Alloys Compd. **813**, 152242 (2020).

[32] Y. Harashima, K. Terakura, H. Kino, S. Ishibashi, and T. Miyake, First-principles study on stability and magnetism of $NdFe_{11}M$ and $NdFe_{11}MN$ for M = Ti, V, Cr, Mn, Fe, Co, Ni, Cu, Zn, J. Appl. Phys. **120**, 203904 (2016).

[33] P. Bruno, Tight-binding approach to the orbital magnetic moment and magnetocrystalline anisotropy of transition-metal monolayers, Phys. Rev. B **39**, 865 (1989).

[34] T. Miyake and H. Akai, Quantum theory of rare-earth magnets, J. Phys. Soc. Jpn. **87**, 041009 (2018).

[35] G. Wiesinger and G. Hilscher, *Magnetism of Hydrides in Handbook of Magnetic Materials* (Elsevier, Amsterdam, 2008).

[36] I. S. Tereshina, N. V. Kostyuchenko, E. A. Tereshina-Chitrova, Y. Skourski, M. Doerr, I. A. Pelevin, A. K. Zvezdin, M. Paukov, L. Havela, and H. Drulis, $ThMn_{12}$-type phases for magnets with low rare-earth content:

Crystal-field analysis of the full magnetization process, Sci. Rep. **8**, 3595 (2018).

[37] A. Jain, G. Hautier, C. Moore, S. P. Ong, C. Fischer, T. Mueller, A. Persson, and G. Ceder, A high-throughput infrastructure for density functional theory calculations, Comput. Mater. Sci. **50**, 2295 (2011).

[38] A. Jain, S. P. Ong, G. Hautier, W. Chen, W. D. Richards, S. Dacek, S. Cholia, D. Gunter, D. Skinner, G. Ceder, and K. A. Persson, The materials project: A materials genome approach to accelerating materials innovation, APL Mater. **1**, 011002 (2013) (access via http://materialsproject.org).

[39] M. Katter, J. Wecker, C. Kuhrt, L. Schultz, and R. Grossinger, Magnetic properties and thermal stability of $Sm_2Fe_{17}N_x$ with intermediate nitrogen concentrations, J. Magn. Magn. Mater. **117**, 419 (1992).

[40] K. Koyama and H. Fujii, Nitrogen gas–solid reaction process and basic magnetism of the interstitially modified rare-earth 3d transition-metal nitrides $R_2Fe_{17}N_3$ (R = Y, Ce, Nd, Sm) and $Y_2Co_{17}N_3$, Phys. Rev. B **61**, 9475 (2000).

[41] L. Steinbeck, M. Richter, U. Nitzsche, and H. Eschrig, Ab initio calculation of electronic structure, crystal field, and intrinsic magnetic properties of Sm_2Fe_{17}, $Sm_2Fe_{17}N_3$, $Sm_2Fe_{17}C_3$, and Sm_2Co_{17}, Phys. Rev. B **53**, 7111 (1996).

[42] M. Ogura, A. Mashiyama, and H. Akai, Role of N in the permanent magnet material $Sm_2Fe_{17}N_x$, J. Phys. Soc. Jpn. **84**, 084702 (2015).

[43] D. S. Wang, R. Wu, and A. J. Freeman, First-principles theory of surface magnetocrystalline anisotropy and the diatomic-pair model, Phys. Rev. B **47**, 14932 (1993).